The Astrophysical Journal, 691:1479–1493, 2009 February 1 doi:10.1088/0004-637X/691/2/1479

A MEASUREMENT OF LARGE-SCALE PECULIAR VELOCITIES OF CLUSTERS OF GALAXIES: TECHNICAL DETAILS

A. Kashlinsky[1], F. Atrio-Barandela[2], D. Kocevski[3], and H. Ebeling[4]
[1] SSAI and Observational Cosmology Laboratory, Code 665, Goddard Space Flight Center, Greenbelt, MD 20771, USA; alexander.kashlinsky@nasa.gov
[2] Fisica Teorica, University of Salamanca, 37008 Salamanca, Spain
[3] Department of Physics, University of California at Davis, 1 Shields Avenue, Davis, CA 95616, USA
[4] Institute for Astronomy, University of Hawaii, 2680 Woodlawn Drive, Honolulu, HI 96822, USA
Received 2008 June 27; accepted 2008 August 27; published 2009 February 5

ABSTRACT

This paper presents detailed analysis of large-scale peculiar motions derived from a sample of ∼ 700 X-ray clusters and cosmic microwave background (CMB) data obtained with *WMAP*. We use the kinematic Sunyaev–Zeldovich (KSZ) effect combining it into a cumulative statistic that preserves the bulk motion component with the noise integrated down. Such statistic is the dipole of CMB temperature fluctuations evaluated over the pixels of the cluster catalog. To remove the cosmological CMB fluctuations the maps are filtered with a Wiener-type filter in each of the eight *WMAP* channels (Q, V, W) that have negligible foreground component. Our findings are as follows. The thermal SZ (TSZ) component of the clusters is described well by the Navarro–Frenk–White profile expected if the hot gas traces the dark matter in the cluster potential wells. Such gas has X-ray temperature decreasing rapidly toward the cluster outskirts, which we demonstrate results in the decrease of the TSZ component as the aperture is increased to encompass the cluster outskirts. We then detect a statistically significant dipole in the CMB pixels at cluster positions. Arising exclusively at the cluster pixels, this dipole cannot originate from the foreground or instrument noise emissions and must be produced by the CMB photons that interacted with the hot intracluster gas via the SZ effect. The dipole remains as the monopole component, due to the TSZ effect, vanishes within the small statistical noise out to the maximal aperture where we still detect the TSZ component. We demonstrate with simulations that the mask and cross-talk effects are small for our catalog and contribute negligibly to the measurements. The measured dipole thus arises from the KSZ effect produced by the coherent large-scale bulk flow motion. The cosmological implications of the measurements are discussed by us in the 2008 work of Kashlinsky et al.

Key words: cosmology: observations – cosmic microwave background – early universe – large-scale structure of universe – methods: numerical – methods: statistical

Online-only material: color figures

1. INTRODUCTION

In the popular gravitational instability picture for growth of the large-scale structure in the universe, peculiar velocities on large cosmological scales probe directly the peculiar gravitational potential and provide important information on the underlying mass distribution in the universe (e.g., see review by Kashlinsky & Jones 1991). Previous attempts to measure the peculiar flows in the local universe mostly used empirically established (but not well understood theoretically) galaxy distance indicators. While very important, such methods are subject to many systematic uncertainties (e.g., see reviews by Strauss & Willick 1995; Willick 2000) and lead to widely different results.

Early measurements by Rubin et al. (1976) indicated large peculiar flows of ∼700 km s^{-1}. A major advance was made using the "fundamental plane" (FP) relation for elliptical galaxies (Dressler et al. 1987; Djorgovski & Davis 1987) with the implication that elliptical galaxies within ∼60 h^{-1} Mpc were streaming at ∼600 km s^{-1} with respect to the rest frame defined by the cosmic microwave background (CMB; Lynden-Bell et al. 1988). Mathewson et al. (1992) used the Tully–Fisher (TF) relation for a large sample of spiral galaxies suggesting that the flow of amplitude 600 km s^{-1} does not converge until scales much larger than ∼60 h^{-1} Mpc. This finding was in agreement with a later analysis by Willick (1999). Employing the brightest cluster galaxies as distance indicators Lauer & Postman (1994) measured a bulk flow of ∼700 km s^{-1} for a sample 119 rich clusters of galaxies on scale of ∼150 h^{-1} Mpc, suggesting significantly larger amount of power than expected in the concordance Λ cold dark matter (ΛCDM) model. However, a reanalysis of these data (Hudson & Ebeling 1997) taking into account the correlation between the luminosities of brightest cluster galaxies and that of their host cluster found a bulk flow in a greatly different direction and at a smaller amplitude. Using the FP relation for early type galaxies in 56 clusters Hudson et al. (1999) find a bulk flow of a similarly large amplitude of ∼630 km s^{-1} as Lauer & Postman (1994) on a comparable scale, but in a different direction. On the other hand, a sample of 24 SNIa shows no evidence of significant bulk flows out to ∼100 h^{-1} Mpc (Riess et al. 1997) and similar conclusion is reached with the TF-based survey of spiral galaxies by Courteau et al. (2000). The directions associated with each bulk-flow measurement are equally discrepant.

The current situation with measurements based on the various distance indicators is confusing and it is important to find alternative ways to measure the large-scale peculiar flows. One way to achieve this is via the kinematic component of the Sunyaev–Zeldovich (SZ) effect produced on the CMB photons from the hot X-ray emitting gas in clusters of galaxies (see review by Birkinshaw 1999). The kinematic SZ (KSZ) effect is independent of redshift and measures the line-of-sight peculiar velocity of a cluster in its own frame of reference. For each individual cluster the KSZ temperature distortion will be small and difficult to measure. Attempts at measuring the peculiar

velocities of individual clusters from the KSZ effect using the current generation of instruments lead to uncertainties of $\gtrsim$1000 km s^{-1} per cluster (see review by Carlstrom et al. 2002). On the other hand, as proposed by Kashlinsky & Atrio-Barandela (2000, hereafter KA-B) for many clusters moving at a coherent bulk flow one can construct a measurable quantity using data on CMB temperature anisotropies which will be dominated by the bulk flow KSZ component, whereas the various other contributions will integrate down. This quantity, the dipole of the cumulative CMB temperature field evaluated at cluster positions, is used in this investigation on the three-year *WMAP* data in conjunction with a large sample of X-ray clusters of galaxies to set the strongest to-date limits on bulk flows out to scales $\sim$300 h^{-1} Mpc.

In the accompanying letter (Kashlinsky et al. 2008) we summed the results and their cosmological implications. These are obtained using the KA-B method applied to three-year *WMAP* CMB data and the largest all-sky X-ray cluster catalog to date. This paper provides the details relevant for the measurement and is structured as follows. Section 2 summarizes the KA-B method and the steps leading to the measurement. Section 3 describes the cluster X-ray catalog used in this study and Section 4 outlines the CMB data processing. Section 5 discusses the methods to estimate the errors, followed by Section 6 with the results on the dipole measurement. Section 7 shows why the measured dipole arises from the KSZ component due to the cluster motion and Section 8 discusses the translation of the measured dipole in μK into velocity in km s^{-1} and its uncertainty. Future prospects foreseeable at this time to improve this measurement are discussed in Section 9. We summarize our results in Section 10.

2. KA-B METHOD AND STEPS TO THE MEASUREMENT

If a cluster at angular position $\vec{y}$ has the line-of-sight velocity v with respect to the CMB, the SZ CMB fluctuation at frequency ν at this position will be $\delta_\nu(\vec{y}) = \delta_{\rm TSZ}(\vec{y})G(\nu) + \delta_{\rm KSZ}(\vec{y})H(\nu)$, with $\delta_{\rm TSZ} = \tau T_{\rm X}/T_{\rm e,ann}$ and $\delta_{\rm KSZ} = \tau v/c$. Here $G(\nu) \simeq -1.85$ to -1.35 and $H(\nu) \simeq 1$ over the range of frequencies probed by the *WMAP* data, τ is the projected optical depth due to Compton scattering, $T_{\rm X}$ is the cluster electron temperature, and $k_{\rm B}T_{\rm e,ann} = 511$ keV. If averaged over many isotropically distributed clusters moving at a significant bulk flow with respect to the CMB, the kinematic term may dominate enabling a measurement of $V_{\rm bulk}$. Thus KA-B suggested measuring the dipole component of $\delta_\nu(\vec{y})$. Below we use the notation for $C_{1,\rm kin}$ normalized so that a coherent motion at velocity $V_{\rm bulk}$ would lead to $C_{1,\rm kin} = T^2_{\rm CMB}\langle\tau\rangle^2 V^2_{\rm bulk}/c^2$, where $T_{\rm CMB} = 2.725$ K is the present-day CMB temperature. For reference, $\sqrt{C_{1,\rm kin}} \simeq 1(\langle\tau\rangle/10^{-3})(V_{\rm bulk}/100\ {\rm km\ s^{-1}})\,\mu$K. When computed from the total of $N_{\rm cl}$ positions the dipole also will have positive contributions from (1) the instrument noise, (2) the thermal SZ (TSZ) component, (3) the cosmological CMB fluctuation component arising from the last-scattering surface, and (4) the various foreground components at the *WMAP* frequency range. The latter contribution can be significant at the two lowest frequency *WMAP* channels (K & Ka) and, hence, we restrict this analysis to the *WMAP* Channels Q, V, and W which have negligible foreground contributions.

For $N_{\rm cl} \gg 1$ the dipole of the observed δ_ν becomes

$$a_{1m} \simeq a^{\rm KSZ}_{1m} + a^{\rm TSZ}_{1m} + a^{\rm CMB}_{1m} + \frac{\sigma_{\rm noise}}{\sqrt{N_{\rm cl}}}. \quad (1)$$

Here $a^{\rm CMB}_{1m}$ is the residual dipole produced at the cluster pixels by the primordial CMB anisotropies. The amplitude of the dipole power is $C_1 = \sum_{m=-1}^{m=1}|a_{1m}|^2$.

Additional contributions to Equation (1) come from nonlinear evolution/collapse of clusters (Rees & Sciama 1968), gravitational lensing by clusters (Kashlinsky 1988), unresolved strong radio sources (present, for instance, in *WMAP* five-year data; Nolta et al. 2008) and the integrated Sachs–Wolfe effect from the cluster pixels. All these effects have a dipole signal only when clusters are inhomogenously distributed on the sky and its amplitude is in turn bounded from above by the amplitude of the monopole. The magnitude of these contributions is at most $\sim$10 μK^2 in power (see Aghanim et al. 2008 for a review on secondary anisotropies) a factor of 10 smaller than the thermal SZ (TSZ) monopole amplitude. Furthermore, as we discuss below, we find a dipole signal when the monopole vanishes, so our measurements cannot be significantly affected by all these effects.

In the following sections we detail out the process that enabled us to isolate the KSZ term in Equation (1). The steps leading to this measurement were:

1. An all-sky catalog of X-ray selected galaxy clusters was constructed using available X-ray data extending to $z \simeq 0.3$.
2. The cosmological CMB component was removed from the *WMAP* data using the Wiener-type filter with the best-fit cosmological model.
3. The filter is constructed (and is different) for each differential assembly (DA) channel because the beam and the noise levels are different. This then prevents inconsistencies and systematic errors that could have been generated if a common filter was applied to the eight channels of different noise and resolution.
4. The filtered CMB maps were used to compute the dipole component at the cluster positions simultaneously as the TSZ monopole vanishes because of the X-ray temperature decrease with radius (Atrio-Barandela et al. 2008, hereafter AKKE; and below).
5. Simulations showed that the measured dipole arises from the cluster pixels at a high confidence level. Since the TSZ component from the clusters vanishes, only a contribution from the KSZ component, due to large-scale bulk motion of the cluster sample, remains.

The following sections present the technical details related to this analysis.

3. X-RAY DATA AND CATALOG

The creation of the all-sky cluster catalog used here from three independent X-ray selected cluster samples is described in detail by Kocevski & Ebeling (2006); for clarity we briefly reiterate the procedure in the following.

The REFLEX catalog consists of 447 clusters with X-ray fluxes greater than 3×10^{-12} erg cm^{-2} s^{-1} in the [0.1–2.4] keV band. The survey is limited to declinations of $\delta < 2.^\circ5$, redshifts of $z \leqslant 0.3$, and Galactic latitudes away from the Galactic plane ($|b| > 20^\circ$). The eBCS catalog comprises 290 clusters in the Northern hemisphere with X-ray fluxes greater than 3×10^{-12} erg cm^{-2} s^{-1} [0.1–2.4] keV at Galactic latitude $|b| > 20^\circ$. The sample is limited to declinations of $\delta > 0^\circ$ and redshifts of $z \leqslant 0.3$ and, like REFLEX, the survey avoids the Galactic plane ($|b| > 20^\circ$). The CIZA sample is the product of the first

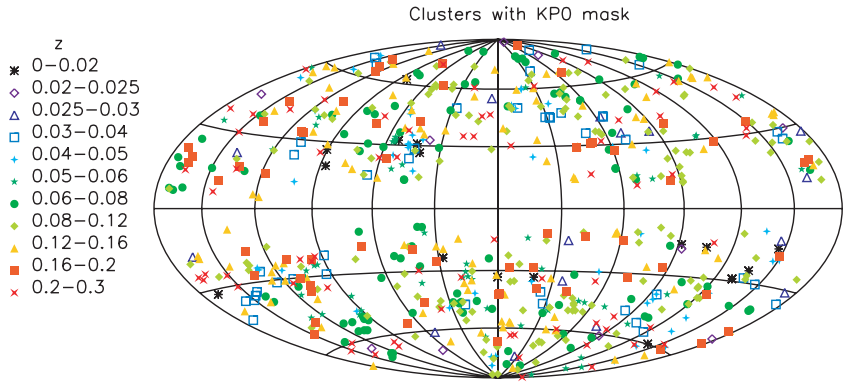

Figure 1. X-ray catalog used in the paper with the KP0 mask applied. Note that at the lowest z clusters have significant N:S asymmetry (for $z \leqslant 0.02$, 0.025, 0.03, 0.04 there are 11:6, 16:11, 24:19, 44:42 N:S clusters), which goes away at $z \gtrsim 0.03$.
(A color version of this figure is available in the online journal.)

systematic search for X-ray luminous clusters behind the plane of the Galaxy. The sample contains 165 clusters with X-ray fluxes greater than 3×10^{-12} erg cm^{-2} s^{-1} [0.1–2.4] keV and redshifts of $z \leqslant 0.3$.

To obtain a single homogeneous sample the physical properties of all clusters were recalculated in a consistent manner using publicly available *ROSAT* All Sky Survey (RASS) data. Cluster positions were redetermined from the centroid of each system's X-ray emission and point sources within the detection aperture are removed. Total X-ray count rates within an aperture of $1.5\,h_{50}^{-1}$ Mpc radius were calculated taking into account the local RASS exposure time and background, and converted into unabsorbed X-ray fluxes in the *ROSAT* broad band [0.1–2.4] keV. Total rest-frame luminosities were determined from the fluxes using the cosmological luminosity distance and a temperature-dependent K-correction. Finally, clusters whose X-ray emission appeared to be dominated by a point source were removed and a flux cut was applied at 3×10^{-12} erg cm^{-2} s^{-1}, leaving 349 REFLEX, 268 eBCS, and 165 CIZA clusters at $z \leqslant 0.3$. The resulting sample is the largest homogeneous, all-sky, X-ray selected cluster catalog compiled to date, containing 782 clusters over the entire sky. Of these, 468 fall within $z \leqq 0.1$. Further details concerning the statistical properties of the catalog, including its completeness, can be found in Kocevski & Ebeling (2006). Figure 1 shows the sky distribution of the clusters used in this analysis.

Our analysis requires knowledge of several parameters describing the properties of the intracluster gas. We determine the X-ray extent of each cluster directly from the RASS imaging data using a growth-curve analysis. The cumulative profile of the net count rate is constructed for each system by measuring the counts in successively larger circular apertures centered on the X-ray emission and subtracting an appropriately scaled X-ray background. The latter is determined in an annulus from $2h_{50}^{-1}$ to $3h_{50}^{-1}$ Mpc around the cluster centroid. The extent of each system is then defined as the radius at which the increase in the source signal is less than the 1σ Poissonian noise of the net count rate. This is essentially the distance from the cluster center at which the X-ray emission is no longer detectable with any statistical significance.

Unabsorbed cluster fluxes were determined from our recalculated count rates by folding the *ROSAT* instrument response against the predicted X-ray emission from a Raymond–Smith (Raymond & Smith 1977) thermal plasma spectrum with 0.3 solar metallicity and by taking into account Galactic absorption in the direction of the source. The temperature used in the spectral model is determined iteratively using the cluster redshift, a first-order approximation on the cluster luminosity using $k_{\rm B}T_{\rm X} = 4$ keV and the $L_{\rm X} - T_{\rm X}$ relation of White et al. (1997). Total rest-frame [0.1–2.4] keV band cluster luminosities were subsequently determined from our recalculated fluxes using the standard conversion with the cosmological luminosity distance and a temperature-dependent K-correction.

To obtain an analytical parametrization of the spatial profile of the X-ray emitting gas and, ultimately, the central electron density we fit a β model (Cavaliere & Fusco-Femiano 1976) convolved with the RASS point-spread function to the RASS data for each cluster in our sample: $S(r) = S_0[1+(r/r_c)^2]^{-3\beta+1/2}$, where $S(r)$ is the projected surface-brightness distribution and S_0, r_c, and β are the central surface brightness, the core radius, and the β parameter characterizing the profile at large radii, respectively. Using the results from this model fit to determine the gas-density profile assumes the gas to be isothermal and spherically symmetric. In practice, additional uncertainties are introduced by the correlation between r_c and β, which makes the results for both parameters sensitive to the choice of radius over which the model is fit, and the fact that for all but the most nearby clusters the angular resolution of the RASS allows only a very poor sampling of the surface-brightness profile (at $z > 0.2$ the X-ray signal from a typical cluster is only detected in perhaps a dozen RASS image pixels). In recognition of these limitations, we hold β fixed at the canonical value of 2/3 and only allow r_c to vary (Jones & Forman 1984). As a consistency check, we also calculate r_c values from each cluster's X-ray luminosity using the $r_c \propto L_{\rm X}^{1/3.6}$ empirical relationship determined by Reiprich & Böhringer (1999). Our best-fit values for r_c are reassuringly robust in the sense that we find broad agreement with the empirically derived values.

Our best-fit parameters, the cluster luminosity and electron temperature, are used to determine central electron densities for each cluster using Equation (6) of Henry & Henriksen (1986) with the temperature of the intracluster medium (ICM) being estimated from the $L_{\rm X}$–$T_{\rm X}$ relationship of White et al. (1997). The electron densities are in turn used to translate the CMB dipole in μK into an amplitude in km s^{-1} as described below. We also calculated electron densities using our empirically derived cluster parameters and find good agreement between the resulting dipole amplitude and the amplitude obtained using our best-fit values.

The distribution of the cluster radial extents determined by the X-ray emission, $\theta_{\rm X-ray}$, for our catalog is shown in Figure 2. Coma at $z \simeq 0.02$ has the largest extent $\theta_{\rm X-ray} \simeq 35'$. In

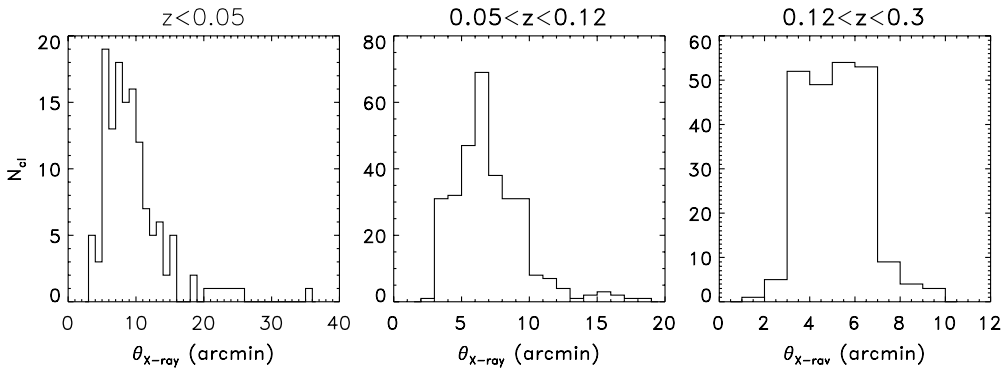

Figure 2. Distribution of cluster X-ray extent in various z-bins using the KP0 maps. Coma is the only cluster with X-ray radial extent larger than 0.5 deg.

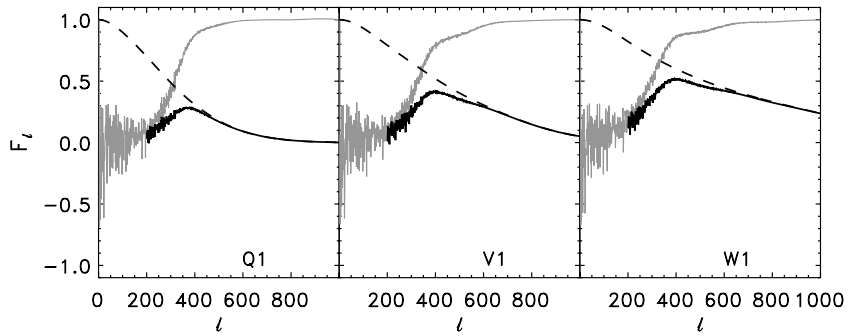

Figure 3. Filters used in removing the cosmological CMB fluctuations are shown with light-shaded lines. Dashed lines show the beam profiles for the marked *WMAP* channels. Solid lines show the product of the two: $B_\ell F_\ell$.

order to avoid the few large clusters, such as Coma, biasing the determination of the dipole, we introduce a cutoff of 30′ in the net extent when increasing the size to account for the extent of the SZ producing gas. The final analysis was made increasing cluster X-ray extent to $6\theta_{\rm X-ray}$ and then cutting them at 30′ to ensure robust dipole computation. In the process, the variations in the cluster size across the sky become greatly reduced; e.g., for the entire sample of 674 clusters that survive the KP0 CMB mask, the final mean radial extent of the clusters is 28.′4, standard deviation is 3.′2, and only 16 clusters have radii below 20′. Thus in our final measurements all clusters are effectively 30 arcmin in radius independently of the cluster position.

Conversions between angular extents and the physical dimensions of clusters are made using the concordance cosmology ($\Omega_\Lambda = 0.7, \Omega_{\rm total} = 1, h = 0.7$).

4. CMB DATA PROCESSING AND FILTERING

Our starting point are the three-year *WMAP* "foreground-cleaned" maps[5] in two Q channels (Q1, Q2), two V channels (V1 and V2), and four W channels (W1 through W4). Channels K and Ka contain fairly significant foreground emission and are not considered in this study. Each channel has its own noise of variance σ_n^2 with the Q channels having the lowest noise and the W channels the highest. The beam transfer functions for each channel, B_ℓ, were obtained from the same URL[5]. The beam is also different in each channel with Q1 having the poorest resolution and W4 the highest. Examples of the beam profile are shown in Figure 3. The maps were masked of foreground emitters using the KP2 and KP0 masks.

[5] Available from http://lambda.gsfc.nasa.gov/product/map/current/m_products.cfm.

The resolution of the input maps is set by choosing $N_{\rm side} = 512$ in HEALpix (Gorski et al. 2005). This corresponds to pixels of 4×10^{-6} sr (47.2 arcmin^2) in area or $\theta_p \simeq 6.'87$ on the side. This resolution is much coarser than that of the X-ray maps used for constructing our cluster catalog.

Because cosmological CMB fluctuations are correlated, they could leave a significant variance in the noise component of our measurement (Equation (1)) over the relatively few pixels occupied by the clusters. Of course, this noise component will be the same, within its standard deviation, for any other pixels in the maps, rather than being peculiar to the cluster pixels. Because the power spectrum of this component, $C_\ell^{\Lambda{\rm CDM}}$, is accurately known from *WMAP* studies (Hinshaw et al. 2007), it can be effectively filtered out of the CMB maps, substantially reducing its contribution to the noise budget in Equation (1). This can be achieved with the Wiener filter, which minimizes the mean square deviation from the noise $\langle(\delta T - \delta_{\rm noise})^2\rangle$ (e.g., Press et al. 1986). The Fourier transform of this filter is

$$F_\ell = \frac{C_\ell({\rm sky}) - C_\ell^{\Lambda{\rm CDM}} B_\ell^2}{C_\ell({\rm sky})}, \qquad (2)$$

where C_ℓ(sky) is the Fourier transform of the sky which contains both the ΛCDM component and the instrument noise.

The resulting filters are shown for selected channels in Figure 3 for the best-fit ΛCDM model of the *WMAP* team (http://lambda.gsfc.nasa.gov). The filter function is negative at some of the low ℓ-multipoles because the true CMB power spectrum differs from the theoretical input due to cosmic variance effects. The filter could, in principle, amplify the noise at low ℓ, but this effect is very small. We checked that the filter does not introduce extra variance or correlations. In any case, larger noise levels in the filtered maps would simply increase the errors which are measured directly from the same maps.

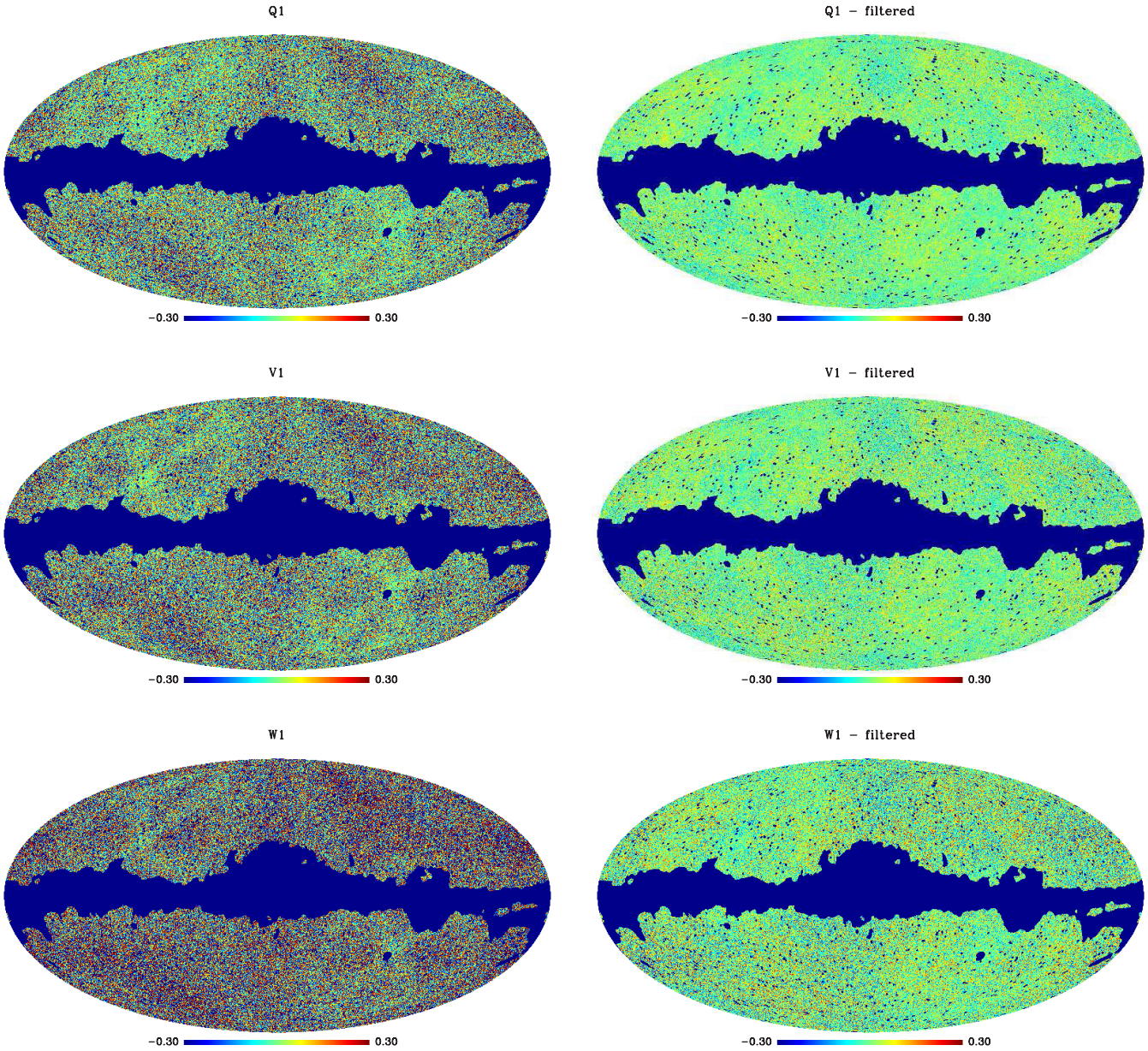

Figure 4. Maps before (left column) and after filtering for the Q1, V1, and W1 channels. The maps are drawn on the same scale. The KP0 mask is shown with dark blue.

(A color version of this figure is available in the online journal.)

Figure 4 shows examples of the original and filtered maps used in our study, and demonstrates that the cosmological CMB component is removed reliably by the adopted filter.

The SZ components too will be affected by the filter. In particular, the intrinsic optical depth of the clusters, determined from X-ray data that have much higher resolution than *WMAP*, should be convolved with the filter in any estimate of the remaining SZ components when using the data from our cluster catalog. Because the X-ray pixels are much smaller, the input τ should also be convolved with the *WMAP* beams. Black lines in Figure 3 show the resulting product, $B_\ell F_\ell$, which determines the final effective τ. The filtering attenuates the τ profile outside $\sim$10 arcmin. More power in τ gets removed in the β model, but filtering will not remove as much power in the more steeply distributed τ such as that which we find in the data.

We demonstrated in a separate study that the extent of the cluster SZ emission significantly exceeds that of the X-ray emission (AKKE). This is not surprising because the SZ effect is $\propto n_e$, whereas for the X-ray luminosity $L_X \propto n_e^2$. However, because of the corresponding decrease in the gas temperature with radius required by this distribution, it does allow us to integrate down the TSZ component by selecting pixels within a larger radius, $\alpha\theta_{\mathrm{X-ray}}$ with $\alpha \geqslant 1$, of the cluster center. We used $\alpha = [1, 2, 4, 6]$ with a cut at $30'$; at the largest extent—when we measure the dipole—the angular extents of clusters become effectively $30'$ across the entire sky. The reasons for TSZ component washing out sooner than the KSZ one are that, as measured by us (AKKE) for the same catalog and CMB data, the cluster X-ray emitting gas is well described by the density profile expected in the ΛCDM model (Navarro et al. 1996, hereafter NFW) and the NFW-distributed gas has X-ray temperature dropping off with radius (e.g., Komatsu & Seljak 2001); this is discussed in some detail later in the paper. When extra pixels (not necessarily belonging to the cluster) are added

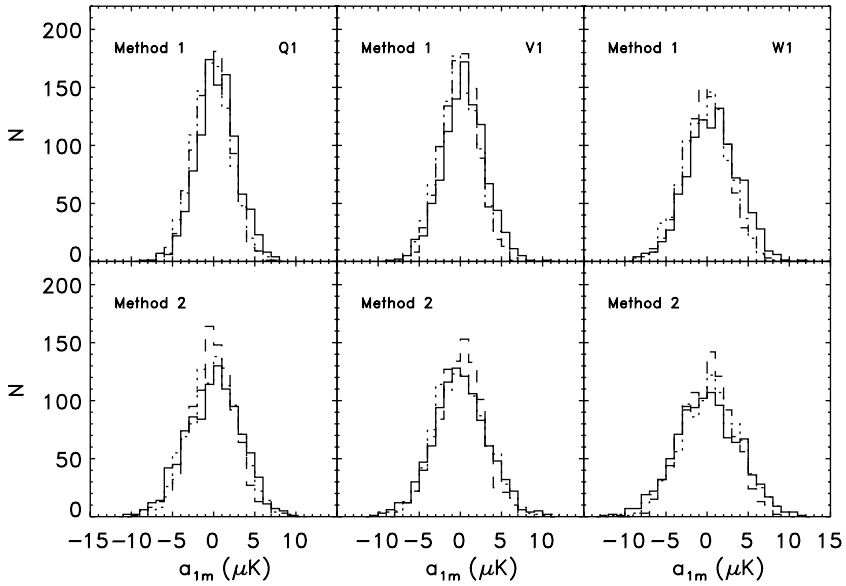

Figure 5. Histograms for simulations for Q1, V1, W1 channels using as input clusters at $z \leqslant 0.05$. Solid lines show the distribution of a_{1x}, dotted for a_{1y} and dashes for a_{1z} from Methods 1 (top panels) and 2. As expected, since the KP0 mask affects most strongly the x-component of the dipole, and least strongly the z-component, the errors on a_{1x} are the largest and on a_{1z} are the smallest. The largest difference between the errors from the two methods is for the x-component, but even there the differences are $\lesssim$ 10%–15%.

in the process it would lead to *decrease* in the accuracy of the dipole determination. Our choice of the maximal extent at $\alpha = 6$ is motivated by the measurement that this roughly corresponds to the maximal extent where the SZ producing gas is detected on average in the *WMAP* data (AKKE). Of course, if we were to increase the total extent further, we should expect that the dipole component due to KSZ should also start decreasing. We verified this by computing the CMB dipole from clusters with the net extent of 1, 2, and 3 degrees. (With this catalog, we cannot go further since the clusters' overlap starts getting in the way; e.g., at 3° the clusters already occupy ∼35% of the available sky). The decrease in the dipole component is discussed in greater detail in Section 7.

Wiener filtering reduces the TSZ temperature decrement and optical depth for each cluster. When extending the analysis up to the largest extent (practically $\simeq 30'$ radius) we find that the TSZ is diluted by noise and reduced to zero. Since clusters are not randomly distributed on the sky the TSZ signal will give rise to a nontrivial dipole signature that, in principle, may confuse the KSZ dipole. Nevertheless, the dipole generated by the cross-talk with the monopole cannot exceed the former, i.e., it must be $a_0^{\rm TSZ} > a_{1m}^{\rm TSZ}$, for all m; it is shown below (Sections 7, 8) that this component is small. The following section describes the results of the various simulations which support this statement.

5. ERROR ESTIMATION

Each of the eight CMB channel maps is processed separately. In the final maps, we set all pixels to zero that fall outside of both the cluster areas and the mask and then compute the dipole for each band using the *remove_dipole* procedure in the standard HEALPix package. Errors are computed from the pixels not associated with clusters as described below. The results from each channel are added after weighting with their respective uncertainties.

We have estimated the errors with two different methods in order to account for both the effects of the KP0 mask and the intrinsic distribution of the cluster samples in different redshift bins. (1) At each z-bin we select new random pixels equal to the number of clusters in each of the eight *WMAP* channel maps. These new pseudocluster centers are iteratively selected to lie outside the KP0 mask and away from any of the true cluster pixels. They are then assigned the cluster radii from the cluster catalog and the *WMAP* pixels are selected within these new pseudoclusters to compute the new dipole. We then ran 1000 realizations computing the errors to within a few percent accuracy. This method accounts for the effects induced by the geometry of the KP0 mask. (2) In the second method, we keep the clusters fixed at their celestial coordinates. The CMB maps for each of the eight channels are then Fourier transformed and their power spectrum C_ℓ computed and corrected for the fraction of the sky occupied by the KP0 mask. We use this power spectrum to generate new random phases in the corresponding $a_{\ell m}$'s, which are then transformed back into the new CMB sky maps, $T_{\rm new}(\theta, \phi)$. In the new sky maps, we select pixels occupied by the real clusters and compute the resulting dipole. This method accounts for the effects induced by the possible leakage from noise and residual CMB due to the intrinsic distribution of the cluster sample in each z-bin.

The two methods give dipoles with zero mean and errors that coincide to within a few percent of each other, which is consistent with the cluster distribution not confusing the final measurement.

Figure 5 shows an example of the distribution of the dipole components from 1000 simulations using random pixel locations in the maps. The figure shows that, as expected, the distribution of a_{1m} is Gaussian with zero mean, and that the cosmological CMB component is removed efficiently. The effects of the CMB mask are such that the largest uncertainty is for the a_{1x} component of the dipole and the smallest is for a_{1z}. From these simulations we find that the noise terms for a_{1m} integrate down approximately as $\propto N_{\rm cl}^{-1/2}\alpha^{-1}$, as expected if the CMB component is indeed efficiently filtered out. Furthermore, we have established that, compared to the first-year *WMAP* data, the uncertainties in a_{1m} have decreased by the expected factor

of $\sqrt{3}$. Since the noise terms are proportional to $t^{-1/2}$, the final eight-year *WMAP* data should further improve the measurement.

In order to assess that there is no cross-talk between the remaining monopole and dipole which may confuse the measured KSZ dipole, we conducted the following experiment. (1) The TSZ and KSZ components from the catalog clusters were modeled as described in Section 8. To exaggerate the effect of the cross-talk from the TSZ component, the latter was normalized to the *maximal* measured monopole for the bins where a statistically significant dipole is detected (-1.3 μK after filtering; for comparison Figure 6 shows the results for the entire catalog, where the measured monopole is 0 ± 0.2 μK). For the KSZ component each cluster was given a bulk velocity, $V_{\rm bulk}$, in the direction specified in Table 2, whose amplitude varied from 0 to 3000 km s^{-1} in 31 increments of 100 km s^{-1}. The resultant CMB map was then filtered and the CMB dipole, a_{1m}(cat), over the cluster pixels computed for each value of $V_{\rm bulk}$. (2) At the second stage we randomized cluster positions with (l, b) uniformly distributed on celestial sphere over the *full* sky for a net of 1000 realizations for each value of $V_{\rm bulk}$ (31,000 in total). This random catalog keeps the same cluster parameters, but the cluster distribution now occupies the full sky (there is now no mask) and on average does not have the same levels of anisotropy as the original catalog. We then assigned each cluster the same bulk flow and computed the resultant CMB dipole, a_{1m}(sim), for each realization. The final a_{1m}(sim) were averaged and their standard deviation evaluated. Figure 6 shows the comparison between the two dipoles for each value of $V_{\rm bulk}$. One can see that there is no significant offset in the CMB dipole produced by either the mask or the cluster true sky distribution. The two sets of dipole coefficients are both linearly proportional to $V_{\rm bulk}$ and to each other; in the absence of any bulk motion we recover to a good accuracy the small value of the TSZ dipole. The most noticeable offset is for the x-component of the dipole which is most affected by the mask, but even here the absolute value of that offset is negligible. In principle, since the bulk flow motion is fixed in direction and the cluster distribution is random, one expects the calibration factor defined in Section 8, $C_{1,100}$, which translates the dipole in μK into velocity in km s^{-1}, to be different from one realization to the next, e.g., in some realizations certain clusters may be more heavily concentrated in a plane perpendicular to the bulk flow motion and the measured $C_{1,100}$, would be smaller. In our case, the mean $C_{1,100}$ differs by $\lesssim 10\%$ suggesting that our catalog cluster distribution is close to the mean cluster distribution in the simulations. This difference in the overall normalization would only affect our translation of the dipole in μK into $V_{\rm bulk}$ in km s^{-1}.

Finally, we note that the errors computed this way are largely uncorrelated. For each subsequent z-bin we add significantly more new cluster pixels, but the computed dipole, of course, includes the clusters in the preceding bins. On the other hand, the errors are computed from random positions on the maps and every realization contains, on average, a completely new set of pixels. There may be some correlations between the various dipole component errors produced by the mask, but as Figures 5 and 6 show these correlated components of the errors are small.

6. RESULTS

6.1. Results by Frequency Band

Section 6.2 shows the measured dipole in the various redshift bins and shells for each of the three frequency channels (Q, V, W), combining the numbers from each of the DAs with weights obtained from the simulations. There the dipole amplitude is such that the measurement becomes statistically significant for $N_{\rm cl} \gtrsim 300$ for the *WMAP* data noise levels. The dipole appears at the negligible monopole component when computed from the clusters *WMAP* pixels. By itself this shows that it cannot originate from the TSZ component. Nevertheless, here we also briefly discuss its spectral energy distribution in as far as it relates to the KSZ origin of the measured dipole.

The KSZ and TSZ components have different frequency dependence potentially allowing us to distinguish the two origins of the measured dipole. When CMB photons are scattered by the hot X-ray gas, the evolution of their occupation number, n, is described by the Kompaneets Equation, $\frac{\partial n}{\partial y} = \frac{1}{x^2}\frac{\partial}{\partial x}\left[x^4\left(\frac{\partial n}{\partial x} + n + n^2\right)\right]$. Here $x \equiv h_{\rm P}\nu/k_{\rm B}T_{\rm CMB}$ and y is the comptonization parameter. In the limit of $y \ll 1$ and for the initially black body radiation, $n = 1/[\exp(x) - 1]$, this equation specifies the change in the photon spectrum as (e.g., Stebbins 1997)

$$\Delta n \simeq y \frac{x\exp(x)}{[\exp(x)-1]^2}\left[x\coth\frac{x}{2} - 4\right]. \quad (3)$$

As expected, the distortion, Δn, vanishes at high-frequency limit ($x \to \infty$). The *WMAP* measurement data are in thermodynamic temperature units, so the TSZ spectrum is given by $\Delta T_{\rm TSZ}/T_{\rm CMB} = yG(x)$ with

$$G(x) = x\coth\left(\frac{x}{2}\right) - 4. \quad (4)$$

The expression gives $G(x)$ which is close to -2 for low frequencies, vanishes near 217 GHz, goes positive at higher frequencies decreasing to zero again at the highest frequencies. Additionally, there may be nonthermal components and relativistic corrections (Birkinshaw 1999).

Similarly, the KSZ spectrum can be shown to be given by $\Delta T_{\rm KSZ}/T_{\rm CMB} = \tau\frac{v}{c}H(x)$ (Phillips 1995) with

$$H(x) = 1. \quad (5)$$

Note that the form of the SZ terms, Equations (4)–(5), changes if CMB properties are expressed via the antenna, rather than thermodynamic temperature.

The dipole values in Table 1 are flat across the *WMAP* frequencies, from 40 to 94 GHz and are consistent with the spectrum expected from the KSZ component, although the present data also give acceptable χ^2 for the TSZ spectrum. Decreasing the noise by $\sim$2 expected from the future *WMAP* measurements may help to distinguish the two components.

As a further consistency check and to estimate how much of the signal is contributed by the farthest clusters, we have also computed the numbers in a shell configuration excluding clusters with $z \leqslant 0.05$ and for the 274 clusters with $0.12 \leqslant z \leqslant 0.3$. Interpretation of such numbers can be cumbersome because of the complicated window involved, but nevertheless they can provide a useful diagnostic of the consistency of the results and the contribution to the dipole by the farthest clusters. Our results show that we start getting statistically meaningful results with at least $\sim$300 clusters, so the runs were done for the bins where the outer z exceeded 0.012. The dipole coefficients for each band are shown in the last three columns of Table 1. They are overall consistent with the main results and provide further support that the dipole is generated by cluster motions on the largest scales.

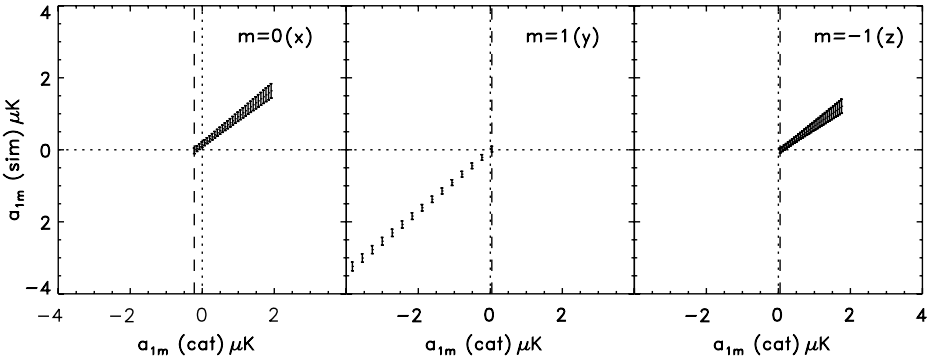

Figure 6. The dipole coefficients for simulated cluster distribution (random and, on average, isotropic) are compared to that from the true catalog (see the text for details). Each cluster in each catalog is given bulk flow of $V_{\rm bulk}$ from 0 to 3000 km s^{-1} in increments of 100 km s^{-1} toward the apex of the motion from Table 2. The results from 1000 simulated catalog realizations were averaged and their standard deviation is shown in the vertical axis. Dotted lines mark the zero dipole axis of the panels. Dashed vertical lines show the dipole due to the modeled TSZ component.

Table 1
Results from Q, V, W Filtered Maps

$z \leqslant$	Band	Multipoles				Shells: $0.05 < z \leqslant$ & $0.12 < z \leqslant 0.3$		
		$\langle \Delta T \rangle$ μK	$a_{1,x}$ μK	$a_{1,y}$ μK	$a_{1,z}$ μK	$a_{1,x}$ μK	$a_{1,y}$ μK	$a_{1,z}$ μK
0.05	Q	−0.1 ± 0.9	−1.0 ± 1.7	−3.6 ± 1.6	0.0 ± 1.5	...	...	...
...	V	0.8 ± 1.0	−1.3 ± 1.8	−2.9 ± 1.6	−0.2 ± 1.5	...	...	...
...	W	−0.4 ± 0.9	−0.3 ± 1.7	−3.2 ± 1.5	0.1 ± 1.4	...	...	...
0.06	Q	−1.0 ± 0.8	−0.4 ± 1.5	−2.6 ± 1.3	−0.7 ± 1.3	...	...	...
...	V	−0.0 ± 0.8	−1.1 ± 1.5	−2.2 ± 1.4	−0.9 ± 1.3	...	...	...
...	W	−1.6 ± 0.7	−1.5 ± 1.4	−2.2 ± 1.3	0.1 ± 1.2	...	...	...
0.08	Q	−1.1 ± 0.7	1.8 ± 1.2	−1.4 ± 1.1	−1.6 ± 1.0	...	...	...
...	V	−0.5 ± 0.7	1.5 ± 1.2	−1.6 ± 1.1	−1.2 ± 1.0	...	...	...
...	W	−2.1 ± 0.6	0.5 ± 1.1	−1.5 ± 1.0	−0.5 ± 0.9	...	...	...
0.12	Q	−0.8 ± 0.5	1.4 ± 1.0	−1.8 ± 0.9	−0.6 ± 0.8	2.8 ± 1.2	−0.9 ± 1.1	−0.9 ± 1.0
...	V	−0.3 ± 0.5	1.7 ± 1.0	−2.2 ± 0.9	−0.4 ± 0.9	3.7 ± 1.2	−1.8 ± 1.1	−0.4 ± 1.0
...	W	−1.1 ± 0.5	1.4 ± 0.9	−2.5 ± 0.8	−0.2 ± 0.8	2.7 ± 1.1	−2.2 ± 1.0	−0.5 ± 0.9
0.16	Q	−0.1 ± 0.5	0.8 ± 0.9	−2.6 ± 0.8	−0.1 ± 0.8	1.6 ± 1.0	−2.2 ± 0.9	−0.2 ± 0.9
...	V	0.4 ± 0.5	1.1 ± 0.9	−2.6 ± 0.8	0.4 ± 0.8	2.3 ± 1.1	−2.6 ± 0.9	0.6 ± 0.9
...	W	−0.4 ± 0.4	0.1 ± 0.9	−3.5 ± 0.8	0.2 ± 0.7	0.5 ± 1.0	−3.7 ± 0.9	0.1 ± 0.8
0.20	Q	−0.0 ± 0.5	1.0 ± 0.9	−2.9 ± 0.8	0.3 ± 0.7	1.8 ± 1.0	−2.7 ± 0.9	0.5 ± 0.8
...	V	0.5 ± 0.5	1.1 ± 0.9	−2.8 ± 0.8	0.7 ± 0.7	2.2 ± 1.0	−2.9 ± 0.9	1.0 ± 0.8
...	W	−0.2 ± 0.4	0.2 ± 0.8	−4.1 ± 0.7	0.6 ± 0.7	0.6 ± 0.9	−4.4 ± 0.9	0.6 ± 0.8
0.30	Q	−0.1 ± 0.4	0.9 ± 0.8	−2.2 ± 0.7	0.4 ± 0.7	1.6 ± 0.9	−1.9 ± 0.8	0.5 ± 0.8
...	V	0.4 ± 0.4	1.2 ± 0.9	−2.2 ± 0.8	0.7 ± 0.7	2.2 ± 0.9	−2.2 ± 0.8	1.0 ± 0.8
...	W	−0.3 ± 0.4	−0.2 ± 0.8	−3.5 ± 0.7	0.5 ± 0.6	0.1 ± 0.9	−3.7 ± 0.8	0.5 ± 0.7
0.12–0.3	Q	...	...	...	...	0.8 ± 1.4	−2.9 ± 1.3	2.3 ± 1.2
...	V	...	...	...	...	0.9 ± 1.5	−2.2 ± 1.3	3.1 ± 1.2
...	W	...	...	...	...	−2.2 ± 1.4	−5.2 ± 1.3	1.9 ± 1.2

Notes. Intermediate results are shown for each of the *WMAP* bands in the redshift bins specified in the first column. Columns 3–6 give the numbers for the standard cluster configuration used in the paper. The last three columns show the dipole in the shell configuration excluding the clusters at $z \leqslant 0.05$. In the latter case, we restricted the runs to when we are left with at least 300 clusters in the shell in order to get statistically meaningful results.

Figure 7 plots the dipole amplitude for four farthest redshift bins versus the frequency of each channel juxtaposed against the TSZ energy spectrum normalized via the least-squares regression. The TSZ spectrum (Equation (4)) would predict a smaller dipole value in the W band. On the other hand, the spectrum of the dipole arising from the KSZ should be flat across the frequencies consistent with the plotted numbers (as mentioned above and shown in the figure the TSZ spectrum also gives acceptable χ^2 given the noise in the present *WMAP* data).

6.2. Results Averaged Over All Frequency Channels

Table 2 shows the results after weight averaging over all of the eight channels. The table also gives additional information on the cluster samples used in each measurement. In order to assess the potential impact of cooling flows on the results, we have also made the computations omitting cluster central pixels in *WMAP* data. The results were essentially unchanged compared to those presented in the table. There is a clear statistically significant dipole at the level of ∼2–3 μK once we reach ∼300 clusters and the aperture ($\simeq 30'$) encompassing most of the hot gas producing the SZ effect. The dipole remains as the monopole representing the mean TSZ component from hot gas within the selected aperture vanishes.

The direction of the dipole and its uncertainty in Table 2 were computed as follows. Each dipole component is assumed to be Gaussian distributed, with the given mean and errors. At each z we generate 10^4 dipoles from a normal distribution with the standard deviation equal to each component error bar and compute the angle of these dipoles with respect to the direction

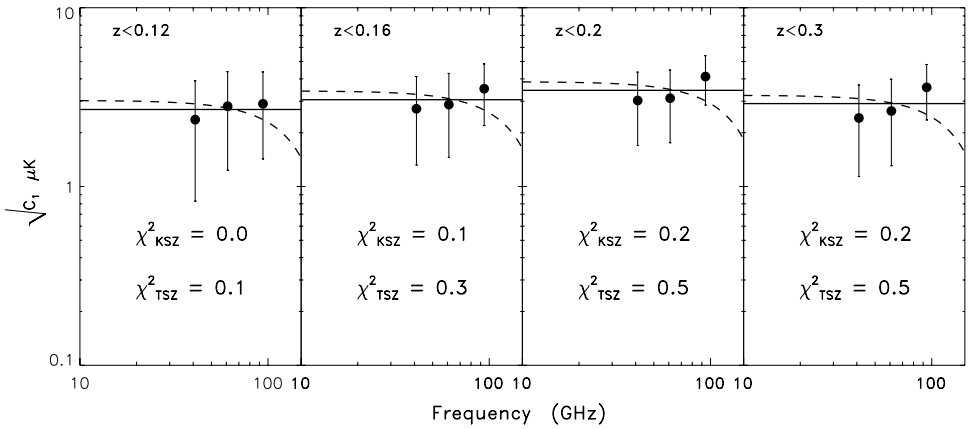

Figure 7. Spectral energy distribution of the measured dipole amplitude vs. the frequency of each of the *WMAP* Q, V, W bands. The measured amplitudes are shown with circles and 1σ uncertainties. Solid lines show the spectrum of any KSZ component obtained by minimizing the corresponding χ^2; dashed lines show the same for the TSZ component given by Equation (4). The corresponding χ^2 per two degrees of freedom are also shown in the panels.

Table 2
Cluster and Map Parameters with Results from Averaging Over All Channels

(1) $z \leqslant$	(2) $\langle z \rangle$	(3) $z_{\rm median}$	(4) $N_{\rm cl}$	(5) $N_{\rm pixels}$	(6) $\langle T \rangle$	(7) $a_{1,x}$	(8) $a_{1,y}$	(9) $a_{1,z}$	(10) $\sqrt{C_1}$	(11) (l,b)	(12) $\sqrt{C_{1,100}}$: μK per 100 km s^{-1}	
					μK	μK	μK	μK	μK	deg	(a)	(b)
0.02	0.016	0.016	17	941	−2.6 ± 1.5	−4.4 ± 3.2	2.0 ± 2.9	7.5 ± 2.5	8.9 ± 5.0	n/a	0.18 (0.70)	0.20 (0.84)
0.025	0.018	0.019	27	1,497	−5.2 ± 1.2	−5.5 ± 2.4	−2.9 ± 2.1	0.1 ± 2.0	6.2 ± 3.8	n/a	0.18 (0.70)	0.20 (0.78)
0.03	0.022	0.023	43	2,417	−5.9 ± 1.0	0.3 ± 1.9	2.9 ± 1.6	0.5 ± 1.6	3.0 ± 2.9	n/a	0.18 (0.73)	0.20 (0.82)
0.04	0.029	0.030	86	4,872	0.5 ± 0.7	−1.6 ± 1.3	0.8 ± 1.1	−2.6 ± 1.1	3.1 ± 2.0	n/a	0.20 (0.73)	0.24 (0.89)
0.05	0.035	0.036	135	7,575	0.1 ± 0.5	−0.8 ± 1.0	−3.3 ± 0.9	−0.0 ± 0.9	3.4 ± 1.6	(256, − 0) ± 24	0.22 (0.76)	0.24 (0.82)
0.06	0.041	0.042	188	10,474	−1.0 ± 0.4	−1.0 ± 0.9	−2.4 ± 0.8	−0.5 ± 0.7	2.6 ± 1.4	(247, − 10) ± 26	0.22 (0.80)	0.22 (0.79)
0.08	0.051	0.053	292	16,064	−1.3 ± 0.4	1.3 ± 0.7	−1.5 ± 0.6	−1.1 ± 0.6	2.2 ± 1.1	(310, − 29) ± 24	0.24 (0.76)	0.26 (0.83)
0.12	0.067	0.067	444	24,189	−0.7 ± 0.3	1.5 ± 0.6	−2.2 ± 0.5	−0.4 ± 0.5	2.7 ± 0.9	(305, − 9) ± 17	0.26 (0.79)	0.28 (0.88)
0.16	0.080	0.076	541	29,127	−0.1 ± 0.3	0.7 ± 0.5	−2.9 ± 0.5	0.1 ± 0.4	3.0 ± 0.8	(283, 3) ± 13	0.25 (0.75)	0.27 (0.83)
0.20	0.090	0.082	603	32,146	0.1 ± 0.3	0.7 ± 0.5	−3.3 ± 0.4	0.5 ± 0.4	3.4 ± 0.8	(282, 9) ± 11	0.28 (0.84)	0.29 (0.90)
All z	0.106	0.089	674	35,409	0.0 ± 0.2	0.6 ± 0.5	−2.7 ± 0.4	0.6 ± 0.4	2.8 ± 0.7	(283, 11) ± 14	0.29 (0.965)	0.32 (1.01)
0.05-0.3	0.12	0.11	540	29,896	−0.1 ± 0.3	1.2 ± 0.5	−2.6 ± 0.5	0.7 ± 0.4	2.9 ± 0.8	(295, 14) ± 13	0.31 (0.84)	0.33 (0.92)
0.12-0.3	0.18	0.17	230	11,920	1.7 ± 0.4	−0.2 ± 0.8	−3.5 ± 0.7	2.4 ± 0.7	4.2 ± 1.3	(267, 34) ± 15	0.36 (0.89)	0.40 (1.0)

Notes. Results are shown for the KP0 mask only with the SZ cluster extent taken to be min[$6\theta_{\rm X-ray}$, 30′]. All uncertainties correspond to 1σ from Method 1 in Section 5; the errors are from 1000 realizations, so the error uncertainty is $\simeq 4\%$. Method 2 gives identical errors within $\lesssim 10\%$. E.g.: at $z \leqslant 0.05$, where we first recover a statistically significant dipole, the errors from Method 2 are (1.16, 1.09, 0.94) μK for the (x, y, z) dipole; at $z \leqslant 0.3$ they become (0.62, 0.56, 0.46) μK. By the time the results are rounded to one significant digit in the table the two sets have little difference and for brevity only one set of errors is shown. Of course, the monopole errors are the same for the two methods. The columns are: (1)-(3) the upper, mean and median redshift of the cluster bins. (4),(5) The number of clusters and the number of pixels used in evaluating the dipole in each redshift bin. (6) The mean CMB temperature evaluated over the cluster pixels in each bin. (7)-(10) Three dipole components, a_{1m}, and the dipole amplitude, $\sqrt{C_1}$, evaluated over the cluster pixels in each bin. (11) Direction and its uncertainty associated with the CMB dipole shown for the redshift bins where there is a statistically significant (at least 2σ) measurement of $\sqrt{C_1}$. (12) The total dipole amplitude for $V_{\rm bulk}$ = 100 km s^{-1} for filtered and unfiltered (in parentheses) maps determined using r_c and n_e values for each cluster obtained via (a) our best-fit β model to the RASS data and (b) from the empirical relationship as described below The top 11 rows correspond to sphere configurations; the last two rows correspond to clusters in shells. Of the latter, the last shell has median dipole of $\simeq 0.18$ showing that the measured dipole is produced by the outermost clusters at median depth of $\gtrsim 600\,h^{-1}$Mpc. Previously claimed peculiar flows had directions: (1) CMB dipole is in the direction of $(l, b) = (264.^\circ26 \pm 0.^\circ33, 48.^\circ22 \pm 0.^\circ13)$ and after correction for the Local Group motion becomes toward $(l, b) = (276^\circ \pm 3^\circ, 30^\circ \pm 3^\circ)$ (see Strauss & Willick 1995 and references therein); (2) the Great Attractor motion based on the FP distance indicator (Dressler et al. 1987; Djorgovski & Davis 1987) is toward $(l, b) = (307, 9)^\circ$ (Lynden-Bell et al. 1988); (3) using brightest cluster galaxies as distance indicators by Lauer & Postman (1994) gave motion toward $(l, b) = (343, 52)^\circ$ with uncertainty of $\pm 23^\circ$; (4) Analysis of a sample of spiral galaxies using the TF relation as distance indicator by Willick (1999) suggested motion to $(l, b) = (272, 10)^\circ$ with $\pm 35^\circ$ uncertainty; (5) ref. Hudson et al. (1999) use early galaxy sample for 56 clusters and find motion to $(l, b) = (260 \pm 15, -1 \pm 12)^\circ$.

of the mean dipole. For small angles, this angle follows a χ^2 distribution with 3 degrees of freedom; the uncertainty in the table corresponds to the 68% confidence contour of this distribution. The directions from previous measurements of peculiar flows based on galaxy distance indicators and those of the acceleration dipoles of the various cluster studies are summarized in the note to Table 2. The direction of the bulk flow deduced here is $\sim 20^\circ$ from the "global CMB dipole" direction, with a 1σ error of $\sim 10^\circ$–25° over the range of z probed in this study, and does not vary significantly within the range covered by our data.

The reality of the measured dipole can also be seen from the following. In Figure 8 we present the measured signal of the entire cluster sample ($z \leqslant 0.3$) plotted against X, the cosine of the angle between the detected dipole and the cluster itself for three channels at three different frequencies (Q1, V1, W1). For each cluster the CMB temperature was averaged over the cluster pixels out to min[$6\theta_{\rm X}$, 30′]. Results from linear fits (thick

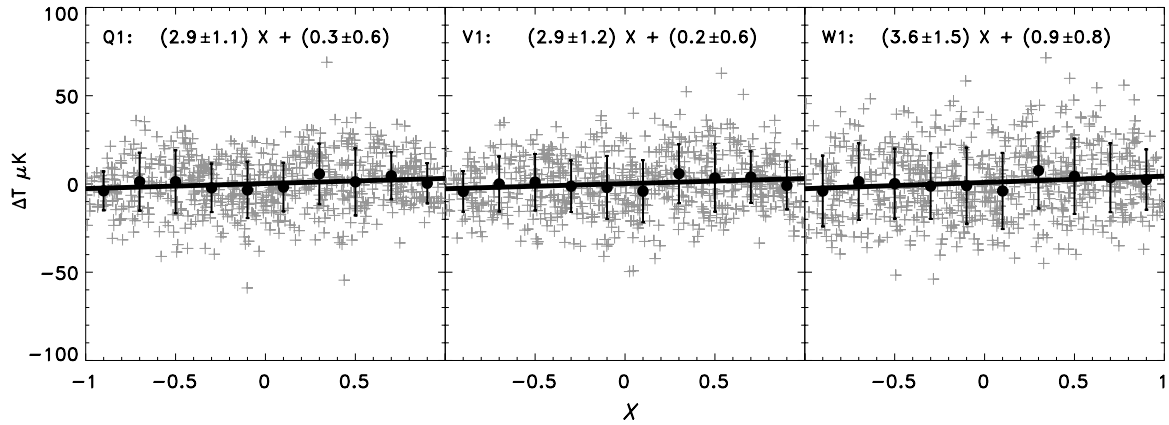

Figure 8. CMB temperature (light shaded plus signs) for each of 674 clusters out to $z \leqslant 0.3$ is plotted vs. X, the cosine of the angle between the dipole apex and each cluster. The plots are shown for one channel at each frequency. The linear fit to the data is shown with thick solid line; its parameters and their uncertainties are displayed at the top of each panel. The uncertainties in the displayed fits were computed using uniform weighting. Filled circles with errors show the mean and standard deviation over all clusters binned in 10 equally spaced bins in X. The correlation coefficient of the binned data shown with circles, $r = \mathrm{cor}(X, \Delta T)$, is 0.5 in Q1 and V1 bands and 0.6 in W1 band. For the unbinned data the correlation coefficient is $\simeq 0.1$ in each of the channels, whereas the random uncorrelated data would give $r = 0$ to within $1/\sqrt{N_{\rm cl}} = 0.038$; this is another way of saying that we detect the dipole at $\sim 2.5\sigma$ level at each channel.

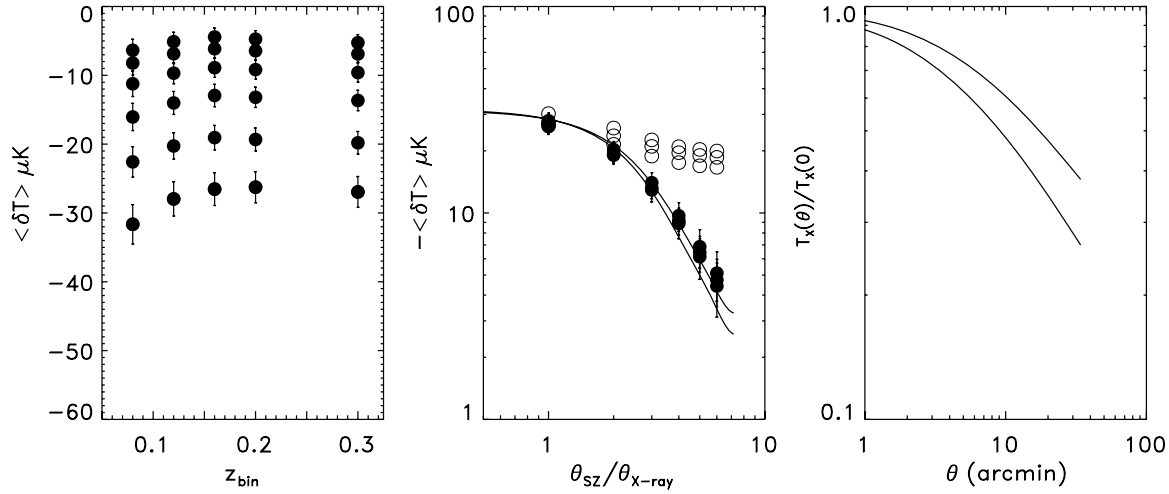

Figure 9. Left: The mean CMB temperature decrement averaged over the Q, V, W channels. The results are for unfiltered maps with 0.°5 cut in cluster extent shown for the outer z-bins for progressively increasing $\alpha = \theta_{\rm SZ}/\theta_{\rm X-ray}$. Filled circles from bottom to top correspond to $\alpha = 1, 2, 3, 4, 5, 6$. Middle: Solid circles show the mean TSZ decrement profile in the unfiltered CMB data vs. α for three farthest z-bins. Open circles correspond to the isothermal $\beta = 2/3$ model evaluated as described in Section 8. The two solid lines correspond to the NFW profile with concentration parameter $c = 6, 10$ normalized to the mean cluster parameters (see AKKE for details). The measured decrease in the filtered TSZ monopole is shown in Figure 1 of Kashlinsky et al. (2008). Right: the X-ray temperature profile in units of the temperature at the center for the NFW profiles shown in the middle panel. The angular scale θ in arcmin corresponds to the average X-ray extent of our cluster sample. That is, the NFW profile corresponds to a single cluster of virial radius 2 h^{-1} Mpc located at an angular distance $d_A = 250\ h^{-1}$ Mpc.

solid lines) to the data and their uncertainties are displayed in each panel. As expected there is a statistically significant dipole component in the cluster CMB temperatures. In each of the eight channels the significance is $> 2\sigma$ leading to the overall result in the main text. The signal is consistent with the spectrum expected from the KSZ component.

7. TSZ MONOPOLE VERSUS KSZ DIPOLE AND RELATED ISSUES

We demonstrate in AKKE that our cluster catalog applied to the *unfiltered* CMB data indicates that the gas in X-ray clusters is well described by the NFW density profile that is theoretically expected from the nonlinear evolution of the concordance ΛCDM model. In addition to using unfiltered maps, the analysis of that paper was done without imposing the 30′ cut on the maximal cluster extent, defined a different effective cluster angular scale and the table there shows the monopole averaged over all the DAs with very different angular resolution diluting the underlying true TSZ signal. Hence, here we revisit their conclusions for the data set used throughout this measurement. In the left panel of Figure 9, we show the mean TSZ decrement at the cluster positions evaluated from the *WMAP* maps for the various total cluster extent limits described in Section 3 (as discussed, the maximal extent here is truncated at 30′). The errors are standard deviations of the CMB temperature evaluated with 1000 random realizations of pseudoclusters over the CMB map pixels outside the mask and away from the catalog clusters. The mean temperature decrement from each of the eight channels were weight averaged with their corresponding uncertainties to give the final $\langle \delta T \rangle$ shown in the figure. The strong decrease in the mean TSZ decrement with the increasing angular size is apparent from the figure.

The middle panel of the figure shows the mean CMB temperature profile of the TSZ decrement in the unfiltered maps for three outer redshift bins. The decrease of the filtered TSZ decrement profile is shown in Figure 1 of Kashlinsky et al.

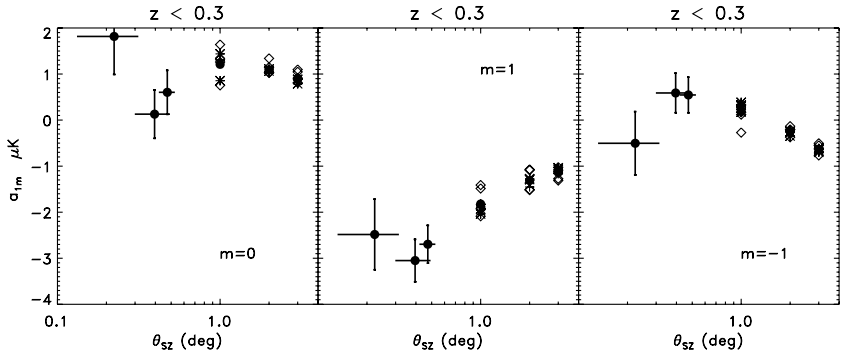

Figure 10. Shows the dipole variation with increasing cluster extent. The cluster electron density profile is such that within the statistical uncertainties the dipole does not change significantly out to the cluster virial radius, where we still detect statistically significant TSZ component as shown in Figure 9. At larger radii it starts decreasing as expected, although if there was some hot gas around the clusters the decrease would be slower. The last three sets of points show the dipole as all clusters are set to extend to 1, 2, and 3 degree radii; the first three correspond to $\alpha = 2, 4, 6$ and the maximal extent set at 0.5 degrees as shown in Figure 1 of Kashlinsky et al. (2008). Pluses correspond to the two Q channels, asterisks to the two V channels, and diamonds to the four W channels. Filled circle shows the mean over all eight channels. The horizontal error bar shows the standard deviation of the cluster radial extent with increasing α. Left panel corresponds to a_{1x} ($m = 0$), middle to a_{1y} ($m = 1$), and right to a_{1z}.

Table 3
TSZ Monopole versus KSZ Dipole Contributions from Rings

Ring	$N_{\rm pixels}$	Monopole (Unfiltered)	Dipole Components (Filtered)		
			$a_{1,x}$	$a_{1,y}$	$a_{1,z}$
		μK	μK	μK	μK
0′–5′	1183	−24.5 ± 9.2	3.5 ± 4.4	−0.9 ± 3.7	−6.2 ± 3.5
5′–10′	3283	−18.0 ± 5.5	1.2 ± 2.6	−4.4 ± 2.2	−5.2 ± 2.1
10′–15′	5546	−12.6 ± 4.3	2.2 ± 2.0	−5.2 ± 1.7	2.9 ± 1.6
15′–20′	7673	−6.8 ± 3.6	0.6 ± 1.7	−4.8 ± 1.5	2.0 ± 1.4
20′–25′	9744	−6.0 ± 3.2	−0.3 ± 1.5	−2.8 ± 1.3	0.5 ± 1.2
25′–30′	11,845	−5.8 ± 2.9	0.9 ± 1.4	−1.0 ± 1.2	−0.3 ± 1.1
30′–45′	47,064	−4.6 ± 1.5	2.7 ± 0.7	−2.0 ± 0.6	1.4 ± 0.6
45′–60′	63,987	−4.3 ± 1.3	0.5 ± 0.6	−0.7 ± 0.5	−0.9 ± 0.5

Notes. Differential contributions to the TSZ monopole (for original maps) and to the KSZ dipole using the lowest resolution W-band (FWHM $\simeq 0.^{\circ}2$) and the entire cluster catalog with $z \leqslant 0.3$ and KP0 mask; the ring width is smaller than the resolution of the Q, V *WMAP* bands. Negative monopole values in the original maps are expected from the TSZ component. The measurements show the existence of the hot intracluster gas out $\gtrsim 30'$ confirming that the dipole is traced by the KSZ component from the cluster gas.

(2008). The expectation from the isothermal β model for these bins was evaluated as described in Section 8 and is shown with the open circles. It fits well the data at the cluster inner parts, but deviates strongly from the measurements at larger radii. The fits from the NFW profiles using a method similar to Komatsu & Seljak (2001) are shown with solid lines for two concentration parameters (see AKKE for details). These profiles provide a good fit to the data.

It is important to emphasize in this context that the gas with the NFW profile, which is in hydrostatic equilibrium with the cluster gravitational field, must have the X-ray temperature decreasing with radius (Komatsu & Seljak 2001). This is confirmed by numerical simulations of the cluster formation within the ΛCDM model (Borgani et al. 2004) as well as by the available observations of a few nearby clusters (Pratt et al. 2007). The latter cannot yet probe the $T_{\rm X}$ profile all the way to the virial radius, but do show a decrease by a factor of ∼2 out to about half of it (see, e.g., Figure 5 of Pratt et al. 2007). In the NFW profile, the gas density profile in the outer parts goes as $n_e \propto r^{-3}$ with the polytropic index, which is approximately constant for all clusters at $\gamma \simeq 1.2$ (Komatsu & Seljak 2001). Thus the X-ray temperature must drop at least as $T_{\rm X} \propto r^{-0.6}$ at the outer parts and for larger values of γ the drop will be correspondingly more rapid. The temperature profile implied by the NFW density profile normalized to the data in the middle panel is shown in the right panel of Figure 9.

The implications of the above are that in the outer parts of clusters the TSZ monopole component must decrease faster than the KSZ dipole as we increase the aperture to probe the cluster outer regions. This is what we observe in the data and it allowed us to isolate the KSZ dipole component as the TSZ monopole vanishes. The reason we present the results out to $\min[6\theta_{\rm X-ray}, 30']$ is that this is roughly the scale where we still detect a statistically significant TSZ signal in the unfiltered data (AKKE; Table 3).

Table 3 shows the differential distribution of the TSZ and dipole components in rings of the specified radius and width around the clusters in our catalog. The data from the W band were selected for the table because this channel has the finest angular resolution making it the most adequate to probe the differential contribution to the final signal. The table clearly shows that in the unfiltered data the X-ray emitting gas producing the TSZ signal exists out to at least 25′–30′, the effective final radius of our cluster catalog. The measurements in the table explicitly confirm that, due to the X-ray temperature decrease, in the filtered maps the dipole KSZ component can be isolated as the TSZ monopole vanishes. Mathematically, discounting the additional $T_{\rm X}$ factor with $\gamma \simeq 1.2$–1.3 in the

Table 4
TSZ Component in Filtered Maps: Observed and Modeled

(1)	(2)	(3)							
	CMB Maps	TSZ Estimate Using Catalogs: (a) | (b)							
$z \leqslant$	$\langle\Delta T\rangle$ μK	$\langle\Delta T\rangle$ μK	$\frac{a_{1,x}}{\langle\Delta T\rangle}$	$\frac{a_{1,y}}{\langle\Delta T\rangle}$	$\frac{a_{1,z}}{\langle\Delta T\rangle}$	$\langle\Delta T\rangle$ μK	$\frac{a_{1,x}}{\langle\Delta T\rangle}$	$\frac{a_{1,y}}{\langle\Delta T\rangle}$	$\frac{a_{1,z}}{\langle\Delta T\rangle}$
0.05	-4.5 ± 1.3	-5.3	0.3	-0.2	-0.2	-5.6	0.2	-0.2	-0.2
0.06	-6.8 ± 1.1	-5.7	0.3	-0.3	-0.2	-6.1	0.3	-0.2	-0.2
0.08	-7.5 ± 1.0	-6.2	0.2	-0.0	-0.1	-6.7	0.2	-0.1	-0.1
0.12	-7.6 ± 0.9	-7.5	0.1	0.0	-0.2	-7.8	0.1	0.1	-0.2
0.16	-7.3 ± 0.8	-7.9	0.2	-0.1	-0.1	-8.6	0.2	-0.0	-0.1
0.20	-7.4 ± 0.8	-8.8	0.1	-0.0	-0.1	-9.75	0.1	-0.0	-0.1
0.30	-7.9 ± 0.8	$-11.$	0.2	-0.0	-0.0	-11.9	0.2	-0.1	-0.0

Notes. Column (1) is the redshift bin of the clusters and (2) shows the observed temperature decrement in the *WMAP* data for $\theta_{SZ} = \theta_{X-ray}$ in each of the bins. Column (3) corresponds to the TSZ temperature decrement and its relative dipole calculated from the X-ray catalog data. In columns (a) and (b) the TSZ temperature decrement is calculated using cluster parameters derived from our best-fit β model to the RASS data and the empirical relationship of Reiprich & Boehringer (1999), respectively. CMB temperature decrements are in μK.

TSZ terms makes the KSZ term for the NFW-like clusters lie close to the TSZ profile of the isothermal $\beta \sim 2/3$ model and, hence, its KSZ decrease with increasing aperture radius should roughly mimic the open circles in the middle panel of Figure 9. Of course, the true cluster properties, such as the electron density and X-ray temperature profiles, can be mathematically constrained (and perhaps even recovered) from the measurements of both the KSZ dipole and TSZ monopole profiles; this, however, lies outside the scope of this investigation.

Of course, as the mean cluster extent gets increased further and we reach past the cluster gas extent radii, we should also observe a decrease in the measured dipole. To check this we have run our pipeline with the net cluster angular extent increased to 1, 2, and 3 degree radii. At the 3° radii the cluster catalog occupies a significant fraction of the available sky, $\simeq 35\%$, so at larger radii the clusters overlapping would become significant. We observe that the dipole, in all z-bins where we have a statistically significant measurement, indeed decreases with the increasing mean extent for the apertures with $\alpha \gtrsim 6$. This is shown in Figure 10. It is interesting to note that as we increase the extent further we may be detecting signs of the two other components of the dipole (x, z), as testified by the small scatter among the mean dipole from all the eight channels. This is because the noise, reflected in the scatter among the eight channels, decreases faster than the dilution factor in the measured dipole. However, it would be difficult to interpret these results with the current version of our X-ray catalog.

8. CALIBRATION: TRANSLATING μK INTO km s^{-1}

In order to translate the CMB dipole in μK into the amplitude of V_{bulk} in km s^{-1}, we proceed as follows. First, we verified that our catalog accurately reproduces the measured TSZ properties of the measured CMB parameters (see also Section 7). Table 4 compares the directly determined TSZ contributions in the redshift bins where we have a statistically significant detection of the dipole with those determined from the parameters in the catalog. The latter is determined as follows. For each cluster we construct a TSZ map in each *WMAP* channel using the catalog values for the electron density, core radius, X-ray temperature and total extent, and assuming $\beta = 2/3$. These maps are then filtered using the filters shown in Figure 3 and coadded using the weights used in the main pipeline. As a consistency check we determine the gas profile using two independent methods: (1) fitting a β profile directly to the RASS X-ray data and (2) using an empirical relationship between the core radius and X-ray luminosity. The quantities derived from the catalog should have the same uncertainties (generated by the CMB maps noise, etc.) as those measured directly and for brevity are not shown. The table shows that there is good agreement between the directly measured TSZ component and that derived using the X-ray cluster catalog for $\theta_{SZ} = \theta_{X-ray}$. The two sets of numbers mostly overlap at 1σ level and always overlap at 2σ. To further check that the agreement is not accidental, we have generated a test catalog randomly assigning the various cluster parameters from different clusters. The agreement completely disappears and the two sets of numbers become different by factors of ~2–3.

Thus the cluster properties in the catalog are determined reasonably well to estimate the translation factor between the CMB dipole amplitude and the bulk flow velocity. To account for the attenuation of the clusters' τ values by both the beam and the filter, we convolve the gas profile of each cluster with the beam and the filter shown in Figure 3 over the *WMAP* pixels associated with it. Each cluster is given a bulk flow motion of 100 km s^{-1} in the direction listed in Table 2, so that each pixel of the ith cluster has $\delta T = T_{CMB}\tau_i(\theta)V_{bulk}/c$, with θ being the angular distance to the cluster center. We then compute the CMB dipole of the resulting cluster map and average the results for each channel map with the same weights as used in the dipole computation. This allows us to estimate the dipole amplitude, $C_{1,100}$, contributed by each 100 km s^{-1} of bulk-flow. We restrict our calculation to the central $1\theta_{X-ray}$ where the β model and NFW profiles differ by 10%–30% and where the central values of the measured dipole are similar to the values measured at the final aperture extent. In other words, we assume that for each cluster all pixels measure the same velocity (in modulus) across the sky, so the calibration constant measured from any subset of pixels is the same irrespective of the signal (in μK) measured at their location.

The results are shown in the last column of Table 2 for the central values of the direction of the measured flow; varying the direction within the uncertainties of (l, b) shown in Table 2 changes the numbers by at most a few percent. A bulk flow of 100 km s^{-1} thus leads to $\sqrt{C_1} \simeq 0.8$ μK for unfiltered clusters; this corresponds to an average optical depth of our cluster sample of $\langle\tau\rangle \simeq 10^{-3}$ consistent with what is expected for a typical galaxy cluster. Filtering reduces the effective τ by a factor of $\simeq 3$. As mentioned above, since a β model provides a poor fit to the measured TSZ component outside the estimated values of θ_{X-ray} (AKKE), we compute $C_{1,100}$ with the total extent assumed to be θ_{X-ray} where the central value of the bulk-flow dipole has approximately the same value as at the final aperture of $\min[6\theta_{X-ray}, 30']$. Owing to the large size of our cluster sample ($N_{cl} \sim 130$–675), the random uncertainties in the estimated values of $C_{1,100}$ should be small, but we cannot exclude a systematic offset related to selection biases affecting our cluster catalog at high redshift. Any such offset, if present, will become quantifiable with the next version of our X-ray cluster catalog which will use the empirically established SZ profile (AKKE) rather than the currently used β model to parameterize the cluster gas profile. The good agreement between the various TSZ-related quantities shown in Table 4 for $\theta_{SZ} = \theta_{X-ray}$ and the observed values for both unfiltered (AKKE) and filtered

maps suggest, however, that these systematic uncertainties are not likely to be high. We also note that they only affect the accuracy of the determination of the amplitude of the bulk flow, but cannot put its existence into doubt, which is established from the CMB dipole detected at the cluster locations. Since the filtering effectively removes the profile outside, approximately, a few arcmin (see Figure 3), it removes a more substantial amount of power in the β model when the cluster SZ extent is increased beyond $\theta_{\rm X-ray}$, than in the steeper profile measured by us (AKKE). Therefore, the effective τ is possibly underestimated by using a β model. Nevertheless, the calibration factor *cannot exceed* $\sqrt{C_{1,100}} \simeq 0.8$ μK given by that of the unfiltered clusters, so the measured flow has bulk velocity of at least a few hundred km s^{-1}, independent of scale, out to at least $\gtrsim 300\ h^{-1}$ Mpc. The above number for the calibration is *lowered* by filtering. Filtering removes somewhat more power in the NFW clusters than in the β model, so the value of $\sqrt{C_{1,100}} = 0.3$ μK for filtered clusters in Table 2, is a firm lower limit. At the same time, the value of the central dipole there is more or less the same as for larger apertures. Figure 6 shows that geometrical considerations do not introduce more that a few percent in the calibration constant.

While the above already limits calibration to a relatively narrow range, a more accurate determination of $C_{1,100}$ would require an adequate knowledge, not yet available, of the NFW profile of each individual cluster. It is not sufficient to know the average profile of the cluster population (AKKE). Filtering acts differently on the NFW-type clusters depending on their angular extent and concentration parameter, i.e., the filtered mean profile is not the same as the mean of all filtered profiles. However, since $C_{1,100}$ was computed using the central pixels, the region where the filter preserves the signal most and where both profiles differ less, we believe that our estimate of $C_{1,100} \simeq 0.3$ μK is fairly accurate, at least in the sense that our overall cosmological interpretation holds within the remaining uncertainties and is fairly independent of the cluster subsamples in Table 2.

9. FUTURE PROSPECTS

The noise of our measurement of the dipole at $1.8(N_{\rm cl}/100)^{-1/2}$ μK with three-year *WMAP* data is in good agreement with the expectations of Kashlinsky & Atrio-Barandela (2000). The uncertainties in our measurement are dominated by the instrument noise and should thus decrease toward the end of the eight-year *WMAP* mission by a factor of $\sqrt{8/3} \simeq 1.6$. This should enable us to measure the flows with an accuracy for individual a_{1m} values of $\simeq 1$ to $\simeq 0.25$ μK for $z \leqslant 0.03$ and $z \leqslant 0.3$, improving the accuracy of the measurement and perhaps uncovering the flows at lower z and the currently undetermined components of the dipole. Particularly useful in the future would be to make such measurement at around 217 GHz, where the TSZ component vanishes, and at larger frequencies, where it changes sign. This could be achievable with the planned ESA-led Planck CMB mission (http://www.rssd.esa.int/planck).

After this project was completed, the *WMAP* mission has released its five-year integration data. The data have lower noise than the three-year integrations used here. We will report the full results from the five-year data analysis (and extended X-ray cluster catalog—see next paragraph) in separate publications after the full work is completed. Suffice it to say here that our preliminary analysis of the five-year CMB maps gives results in full agreement with this paper. However, because the new CMB mask of the five-year data release, KQ75, is somewhat different and larger than the KP0 mask of the three-year data, fewer clusters can enter the final analysis and the reduction in errors seems less than $\sqrt{5/3} = 1.3$. This will be improved with a new expanded cluster catalog that we are developing now as described in the following paragraph.

Another obvious avenue toward improving this measurement goes through an increased cluster sample. Since X-ray selection is critical to ensure that all systems selected are indeed gravitationally bound, and since all-sky (or nearer all-sky) coverage is crucial to ensure unbiased sampling of the dipole field, the database of choice for this purpose remains RASS. The cluster sample used in our present work can be straightforwardly extended by adopting a lower X-ray flux limit. While this will not result in a noticeable increase of our sample at low redshift (at much lower X-ray fluxes than that used here, we would begin to select very poor galaxy groups and even individual galaxies), tremendous statistical gains can still be made at redshifts greater than, say, 0.15 where our present flux limit excludes all but the most X-ray luminous systems. We therefore are working to extend to the whole sky the approach successfully taken by the MAssive Cluster Survey (MACS) project (Ebeling et al. 2001, 2007), i.e., to identify clusters in the RASS data down to detect fluxes of 1×10^{-12} erg cm^{-2} s^{-1} (0.1–2.4 keV), thereby extending our study to redshifts approaching 0.7. We note that the poor photon statistics of the RASS (a detection at such low fluxes consists often of no more than 20 X-ray photons) are irrelevant for our purposes as long as the cluster nature of the X-ray source can be unambiguously confirmed. MACS has demonstrated that this is possible, specifically at high redshift, by means of imaging follow-up observations at optical wavelengths. (Since we recover the CMB dipole, which exists at high significance level only at the CMB pixels associated with X-ray clusters, even adding a small fraction of CMB pixels not associated with true clusters can only decrease the statistical significance of the results rather than introduce bias). Clusters at $z > 0.1$ are essentially unresolved in the RASS, and are most definitely unresolved in the *WMAP* data, meaning that both surveys are sensitive only to the integrated cluster signal which is independent of the exact shape of the X-ray emission (radial surface-brightness profile, general morphology). The compilation of a well defined, RASS-selected, all-sky cluster sample following the MACS selection criteria is currently done by us for this project in conjunction with longer integration *WMAP* data.

We are currently developing ways to improve our calibration of $C_{1,100}$ using a directly fit NFW profile for our catalog clusters. In AKKE, we have measured the average NFW of our cluster sample. The poor resolution of *WMAP* data, the amplitude of the intrinsic CMB signal compared with the TSZ contribution and the limited frequency range of *WMAP* radiometers may limit the ability to estimate the NFW for each individual cluster in our sample using the available CMB data. The PLANCK mission, with its large frequency coverage will allow the estimate of those parameters with enough precision for the purposes of this project. Although our calibration uncertainty is unlikely to exceed ~20%–30%, the newly constructed catalog should narrow down these systematic effects even more.

Further improvements can be done by specifically designing more optimal filtering schemes to specifically isolate the contributions from the clusters of galaxies to CMB anisotropies. Care is required here; our filter is based on the data and the actual realization of the noise. Equation (2) is specifically designed to eliminate the cosmological fluctuations in a given (random

and channel-specific) noise realization, which is done efficiently enough as our results show, because the power spectrum of the largest contributor to the dipole, the cosmological CMB fluctuations, is known with high accuracy. If one uses more theoretical filters, e.g., to isolate the SZ component of the power spectrum, the latter must be known with high accuracy (at least as high as the ΛCDM CMB power spectrum) and it must be known with high accuracy for our catalog clusters. Furthermore, Wiener-type filters do not preserve power and different filters remove different amounts of it. Thus the additional filter-specific issues would be the different calibration procedures and the different monopole (from TSZ) in the residual maps.

10. SUMMARY

We now summarize the main conclusions from this study:

1. Our measurements indicate the existence of the residual CMB dipole evaluated over the CMB pixels associated with the hot SZ producing gas in clusters of galaxies. The dipole is measured at high signifance level ($\sim 8\sigma$ in the outer bins) and persists out to the limit of our cluster catalog $z_{\rm median} \simeq 0.1$. Its direction is not far off the direction of the "global CMB dipole" measured from the entire unprocessed maps.
2. We show with detailed simulation that the CMB mask and/or cluster sample discreteness induced cross-talk effects are negligible and cannot mimic the measured dipole.
3. The dipole originates exclusively at the cluster pixels and, hence, cannot be produced by foregrounds or instrument noise. It must originate from the CMB photons that have passed through the hot gas in the catalog clusters.
4. We prove that the signal arises from the hot SZ producing cluster gas because we demonstrate that in the unfiltered CMB maps there remains a statistically significant temperature *decrement*, as expected from the TSZ effect. Its profile is consistent with the NFW profile out the largest aperture where we still detect hot gas ($\sim 30'$). At larger radii the dipole begins to decrease as expected.
5. In the filtered maps, designed to reduce the cosmological CMB fluctuations, the dipole is isolated simultaneously as the monopole component vanishes. This proves that its origin lies in the KSZ component. The monopole vanishes (within the noise) because for the NFW profile the gas in hydrostatic equilibrium must have a strong decrease in the X-ray temperature in the outer parts. This decrease is consistent with the available direct X-ray measurements, but more importantly is demonstrated empirically in AKKE.
6. With the current cluster catalog we determine that the amplitude of the dipole corresponds to bulk flow of 600–1000 km s^{-1}. This conversion factor, $C_{1,100}$, may however have some systematic offset related to our current cluster modeling. However, this possible uncertainty only affects the amplitude of the motion, not its coherence scale or existence.
7. The cosmological implications are discussed in Kashlinsky et al. (2008). We show there that the concordance ΛCDM model cannot account for this motion at many standard deviations. Instead, it is possible that this motion extends all the way to the current cosmological horizon and may originate from the tilt across the observable universe from far away preinflationary inhomogeneities (Kashlinsky et al. 1994; Turner 1991).

This work is supported by the NASA ADP grant NNG04G089G in the USA (PI: A. Kashlinsky) and by the Ministerio de Educación y Ciencia and the "Junta de Castilla y León" in Spain (FIS2006-05319, PR2005-0359 and SA010C05, PI: F. Atrio-Barandela). We thank Gary Hinshaw for useful information regarding the *WMAP* data specifics. F.A.B. thanks the University of Pennsylvania for its hospitality when part of this work was carried out. We thank Carlos Hernandez-Monteagudo for spotting a technical correction in the SZ energy distribution, Equation (4), and Figure 7.

Note added in proof. Our results have recently received additional support from an independent study by Watkins et al. (2009). The Watkins et al. study compiled all major peculiar velocity surveys to date to determine bulk flows within a 100 h^{-1} Mpc sphere. Although the scales involved are much smaller than, and the method completely different from ours. Watson et al. find that the galaxies within a ∼50–100 h^{-1} Mpc sphere are moving at a significant velocity in the same direction as found in our work. The amplitude of their motion, at ∼400–500 km s^{-1} appears somewhat smaller, but still overlaps within <2 standard deviations with our velocity assuming the calibration above. We anticipate that recalibrating the cluster sample as described in Section 8 will further decrease the difference between the measured velocity amplitudes.

REFERENCES

Aghanim, N., Majumdar, S., & Silk, J. 2008, Rep. Prog. Phys., 71, 066902
Atrio-Barandela, F., Kashlinsky, A., Kocevski, D., & Ebeling, H. 2008, ApJ, Lett., 675, L57 (AKKE)
Birkinshaw, M. 1999, Phys. Rep., 310, 97
Borgani, S., et al. 2004, MNRAS, 348, 1078
Cavaliere, A., & Fusco-Femiano, R. 1976, A&A, 49, 137
Carlstrom, J. E., Holder, G. P., & Reese, E. D. 2002, ARA&A, 40, 643
Courteau, S., et al. 2000, ApJ, 544, 636
Djorgovski, S., & Davis, M. 1987, ApJ, 313, 59
Dressler, et al. 1987, ApJ, 313, 42
Ebeling, H., Edge, A. C., & Henry, J. P. 2001, ApJ, 553, 668
Ebeling, H., et al. 2007, ApJ, 661, L33
Gorski, K., et al. 2005, ApJ, 622, 759
Henry, J. P., & Henriksen, M. J. 1986, ApJ, 301, 689
Hinshaw, G., et al. 2007, ApJS, 170, 288
Holzapfel, W. L., et al. 1997, ApJ, 479, 17
Hudson, M. J., & Ebeling, H. 1997, ApJ, 479, 621
Hudson, M. J., et al. 1999, ApJ, 512, L79
Jones, C., & Forman, W. 1984, ApJ, 276, 38
Kashlinsky, A. 1988, ApJ, 331, L1
Kashlinsky, A., & Atrio-Barandela, F. 2000, ApJ, 536, L67
Kashlinsky, A., Atrio-Barandela, F., Kocevski, D., & Ebeling, H. 2008, ApJ, 686, L49
Kashlinsky, A., & Jones, B. J. T. 1991, Nature, 349, 753
Kashlinsky, A., Tkachev, I., & Frieman, J. 1994, Phys. Rev. Lett., 73, 1582
Kocevski, D. D., & Ebeling, H. 2006, ApJ, 645, 1043
Kocevski, D. D., Ebeling, H., Mullis, C. R., & Tully, R. B. 2007, ApJ, 662, 224
Kocevski, D. D., Mullis, C. R., & Ebeling, H. 2004, ApJ, 608, 721
Komatsu, E., & Seljak, U. 2001, MNRAS, 1353
Lauer, T. R., & Postman, M. 1994, ApJ, 425, 418
Lynden-Bell, D., et al. 1988, ApJ, 326, 19
Mathewson, D. S., Ford, V. L., & Buchhorn, M. 1992, ApJ, 389, L5
Navarro, J. F., Frenk, C. S., & White, S. D. M. 1996, ApJ, 462, 563
Nolta, M. R., et al. 2008, ApJS, in press
Phillips, P. R. 1995, ApJ, 455, 419
Pratt, G. W., et al. 2007, A&A, 461, 71
Press, W. H., Flannery, B. P., Teukolsky, S. A., & Vetterling, W. T. 1986, Numerical Recipes (Cambridge: Cambridge Univ. Press)
Raymond, J. C., & Smith, B. W. 1977, ApJS, 35, 419
Rees, M. J., & Sciama, D. 1968, Nature, 511, 611
Reiprich, T. H., & Boehringer, H. 1999, Astron. Nachr., 320, 296
Riess, A., Davis, M., Baker, J., & Kirshner, R. P. 1997, ApJ, 488, L1
Rubin, V., Roberts, M., Thonnard, & Ford, W. K. 1976, AJ, 81, 719

Stebbins, A. 1997, arXiv:astro-ph/9705178
Strauss, M., & Willick, J. A. 1995, Phys. Rep., 261, 271
Turner, M. S. 1991, Phys. Rev. D., 44, 3737
Watkins, R., Feldman, H. A., & Hudson, M. J. 2009, MNRAS, 392, 743
White, D. A., Jones, C., & Forman, W. 1997, MNRAS, 292, 419
Willick, J. A. 1999, ApJ, 522, 647
Willick, J. A. 2000, in Proc. of the XXXVth Rencontres de Moriond: Energy Densities in the Universe, arXiv:astro-ph/0003232